AIAA JOURNAL
Vol. 46, No. 11, November 2008

Novel Approach to Axisymmetric Actuator Disk Modeling

Aviv Rosen* and Ohad Gur†
Technion–Israel Institute of Technology, Haifa 32000, Israel

DOI: 10.2514/1.37383

Actuator disk models are commonly used for the analysis of rotary wing systems. The blade-element momentum model is probably the most popular one because of its simplicity, efficiency, and good accuracy in many cases. Yet momentum models fail to give satisfactory results in many other cases. The reason is probably the fact that momentum models include a basic assumption that the integral form of the equation of conservation of momentum can be replaced by its differential form. This paper presents a new actuator disk model that does not include the aforementioned assumption. It is assumed that the pressure difference between both sides of each point of the disk is a time average of the pressure difference between both sides of the blade elements that pass through that point. In addition to calculating the axial components of the induced velocity through the disk, the solution procedure also includes calculations of the radial component. The new model includes an iterative solution procedure that converges relatively fast and requires relatively small computing resources and short computing time. The paper describes the new model, presents the solution procedure, and compares the new results with known results from the literature.

Nomenclature

A, B, G, H	=	functions defined in Appendix B
B_{tip}	=	blade tip factor
C	=	factor defined in Eq. (33)
C_d	=	cross-sectional drag coefficient
C_l	=	cross-sectional lift coefficient
C_P	=	power coefficient
$\tilde{C}_P$	=	pressure coefficient
C_{th}, C_T	=	thrust coefficients
c	=	chord, m
$\tilde{c}$	=	equivalent chord, m
D	=	disk diameter, m
D'	=	aerodynamic drag per unit length, N/m
$\mathrm{d}l$	=	blade-element length, m
E	=	complete elliptic integral of the second kind
$\mathbf{e}_r, \mathbf{e}_\psi, \mathbf{e}_z$	=	unit vectors
F_r, F_ψ, F_z	=	components of aerodynamic force per unit length of blade, N/m
I	=	integral defined in Appendix B, m/s
J	=	advance ratio
K	=	complete elliptic integral of the first kind
k	=	pressure ratio factor
L'	=	aerodynamic lift per unit length, N/m
M	=	Mach number
N_b	=	number of blades
n	=	propeller angular frequency, cycles/second
P_r, P_ψ, P_z	=	average components of body force per unit volume, $\mathrm{N/m^3}$
p	=	pressure, $\mathrm{N/m^2}$
p_0	=	correction to p_∞ for pressure at the disk plane, $\mathrm{N/m^2}$
p_∞	=	ambient pressure, $\mathrm{N/m^2}$
Q	=	volumetric flow rate through the disk plane, $\mathrm{m^3/s}$
R	=	disk radius, m
Re	=	Reynolds number
r	=	radial coordinate, m
t	=	time, s
U	=	cross-sectional resultant velocity, m/s
$\mathbf{V}$	=	velocity vector, m/s
V	=	freestream velocity, m/s
v_r, v_ψ, v_z	=	induced velocity components, m/s
w_r, w_ψ, w_z	=	induced velocity components at the disk plane, m/s
x, ξ	=	chordwise coordinate, m
z	=	axial coordinate, m
α	=	angle of attack, rad
γ	=	intensity of the sink distribution per unit area, m/s
Δp	=	pressure difference across the disk, $\mathrm{N/m^2}$
δ	=	Dirac delta function, 1/m
ε	=	small constant
θ	=	cross-sectional pitch angle, rad
$\theta_{0.75}$	=	pitch angle at the three-quarter-blade's cross section, rad
$\kappa, \bar{\kappa}$	=	arguments defined in Appendix B
Λ	=	blade's sweep angle, rad
ρ	=	air density, $\mathrm{kg/m^3}$
φ	=	angle between cross-sectional resultant velocity and the disk plane, rad
ψ	=	circumferential coordinate, rad
ψ_0	=	circumferential location of a blade element at $t = 0$, rad
Ω	=	blade's angular speed, rad/s

Subscripts

l	=	downstream side of the disk ($z = 0^+$)
r	=	radial
u	=	upstream side of the disk ($z = 0^-$)
z	=	axial
ψ	=	circumferential

Superscript

$'$	=	far wake

Received 3 March 2008; revision received 2 June 2008; accepted for publication 13 June 2008.

*Professor, Faculty of Aerospace Engineering; rosen@aerodyne.technion.ac.il. Fellow AIAA.

†Researcher, Faculty of Aerospace Engineering; ohadg@aerodyne.technion.ac.il. Member AIAA.

I. Introduction

THE first model for analyzing rotary wings was the actuator disk model of Rankine and Froude [1] for the analysis of marine propellers. According to actuator disk models, the propeller or rotor

is replaced by an imaginary thin disk that produces discontinuities of properties of the flow through the disk. In spite of the development of more sophisticated and accurate models over the years, including prescribed wake models, free-wake models, and various computational fluid dynamics models, actuator disk models are widely used for the analysis of rotary wing systems. This is because of their simplicity and efficiency on one hand and the relative accuracy that they offer on the other hand. The other more accurate models are usually applied in cases in which a detailed and more accurate solution of the flow is required. Actuator disk models are commonly used for design and flight mechanics simulations, in which efficiency is very important.

Horlock [2] presented an excellent overview of the principles of various actuator disk models and their application to various problems. In what follows, only a brief review will be presented. This is important to understand the advantages of the new model to be presented in the paper.

The best known, and probably the most popular, model is the actuator disk model associated with the momentum theory [3]. It is based on applying the basic principles of conservation of mass, momentum, and energy. The complete model is known as the general momentum model, but there are also various simplified momentum models. However, this model has a major weakness: the integral representing the conservation of axial momentum is replaced by its differential form. Glauert [3] indicated that, "the validity of this equation has not been established and its adoption may imply the neglect of the mutual interference between the various annular elements of the propeller, but the actual deviations from the conditions presented by...are believed to be extremely small in general." The adoption of this assumption may be one of the reasons for the inability of this model to give sufficiently accurate results in various cases.

Thus, although momentum models continued to be applied to an increasing number of problems and in new areas other than aeronautical systems (see, for example, the applications to wind energy problems in [4]), other researchers investigated the inaccuracies associated with this model. As early as 1925, Thoma [5] pointed out inconsistencies within the model. Goorjian [6] showed that when the differential form of the equation of axial momentum is combined with the other equations of the model, it leads to a contradiction. Rauh and Seelert [7] discussed problems with the model associated with Betz theory of optimum efficiency of wind turbines. Van Kuik [8,9] examined the singularity at the edge of an actuator disk and deduced the presence of a singular vortex carrying an edge force. He showed that allowance for this edge force may improve the accuracy of performance prediction of rotors. In a later paper [10], the author continued to discuss the inconsistencies associated with classical actuator disk momentum theory. He ended up by concluding that the origin of the inconsistency is not yet known, and thus it is not clear what changes are required in the modeling of the momentum balance to remove the inconsistencies. More recently, Spalart [11] presented a mathematical model of the flow induced by an actuator disk in axial translation, which is more accurate than the classical solutions. Although performance results of a rotor in hover were unchanged [11], common assumptions were proven to be incorrect, resulting in a different flowfield through the rotor.

The preceding described inconsistencies associated with the classical momentum theory led various researchers to develop accurate actuator disk models [12–19]. The first attempt at solving the nonlinear actuator disk problem was the formulation by Wu [13], though he did not carry out the suggested iterative solution. The first solution of the nonlinear actuator disk problem was that by Greenberg and Kaskel [15] for a uniform blade circulation distribution (and, later, for a piecewise continuous circulation [16]), summarized in [17]. More recently, Conway [20] developed an analytical theory of a linear actuator disk model and then extended it to a heavily loaded actuator disk with nonuniform loading [21]. Although the aforementioned models are accurate because they are based on a solution of the flow equations in the entire flowfield, they are much more complicated and require long computations. Thus, these models lose the main benefit of actuator disk models: namely, their simplicity and efficiency.

Although the present research deals with a nonlinear actuator disk theory for steady axisymmetric flow it should be noted that a major effort in actuator disk analysis has been directed to linearized dynamic inflow models of rotors [22]. These models concentrate on calculating dynamic perturbations of the induced velocities over the disk due to perturbations in the aerodynamic loads along the blades. Of special interest is the work of Morillo and Peters [23] and Peters et al. [24], who showed that a linear potential-flow actuator disk theory can be derived directly from the momentum and continuity equations via the Galerkin approach. Similar to the derivations of the present paper, they showed that one only needs to analyze the pressure on the disk to obtain all three components of flow on and off the disk.

The present paper presents a new actuator disk model, similar in its nature to the momentum model. This new model does not involve a detailed solution of the entire flowfield, but rather concentrates on the flow through the disk and in the far wake. The flow through the disk is modeled by a distribution of sinks that determine the axial and radial components of the induced flow. Only the integral form of conservation of axial momentum is applied, rather than its nonaccurate differential form. The approximation of the present new model includes an assumption about the distribution of the pressure over the disk.

II. Description of the New Model

A rotary wing system (rotor, propeller, wind turbine, etc.) in an incoming axial flow is considered. The system includes N_b identical blades. A cylindrical system of coordinates (r, ψ, z) will be used during the derivations. This is a nonrotating system that is attached to the hub center. The z axis coincides with the axis of rotation and points in the downstream direction, and r and ψ are the radial and angular (azimuthal) coordinates, respectively. It should be noted that ψ is positive in the counterclockwise direction, as seen by an observer located upstream of the hub. For the present axisymmetric case, the rotation direction influences only the direction of the circumferential induced velocity. The blades are rotating with an angular velocity Ω about the z axis. The incoming flow has a velocity V in the positive z direction (as seen by an observer on the rotor hub). The blade root is located at $z = 0$. Thus, the plane $z = 0$ is defined as the plane of rotation.

Because of the action of the blades, velocities are induced over the entire space. The induced velocity at any point is a function of the time t. Thus, the resultant velocity at any point at time t, $\mathbf{V}(r, \psi, z, t)$, equals

$$\mathbf{V}(r, \psi, z, t) = v_r(r, \psi, z, t) \cdot \mathbf{e}_r + v_\psi(r, \psi, z, t) \cdot \mathbf{e}_\psi + [V + v_z(r, \psi, z, t)] \cdot \mathbf{e}_z \tag{1}$$

where $\mathbf{e}_r$, $\mathbf{e}_\psi$, and $\mathbf{e}_z$ are unit vectors in the radial, circumferential, and axial directions, respectively; $v_r(r, \psi, z, t)$, $v_\psi(r, \psi, z, t)$, and $v_z(r, \psi, z, t)$ are the radial, circumferential, and axial components of the induced velocity, respectively. The pressure at any point is $p_\infty + p(r, \psi, z, t)$, where p_∞ is the pressure far from the disk.

The entire flowfield is divided into three main regions: 1) the actuator disk, which is the volume occupied by the rotating blades; 2) the wake, which includes the fluid that has passed through the actuator disk; and 3) the rest of the flowfield. In what follows, these three regions will be considered.

A. Actuator Disk

It is assumed that the blades are slender and the distance between any material point of the blades and the plane of rotation is small compared with the radial coordinate of the same material point. Thus, the thickness of the actuator disk will be neglected.

Each blade is represented by its quarter-chord line (see Fig. 1), which is the line connecting the quarter-chord points of all the cross sections. The blade's cross sections are normal to the quarter-chord

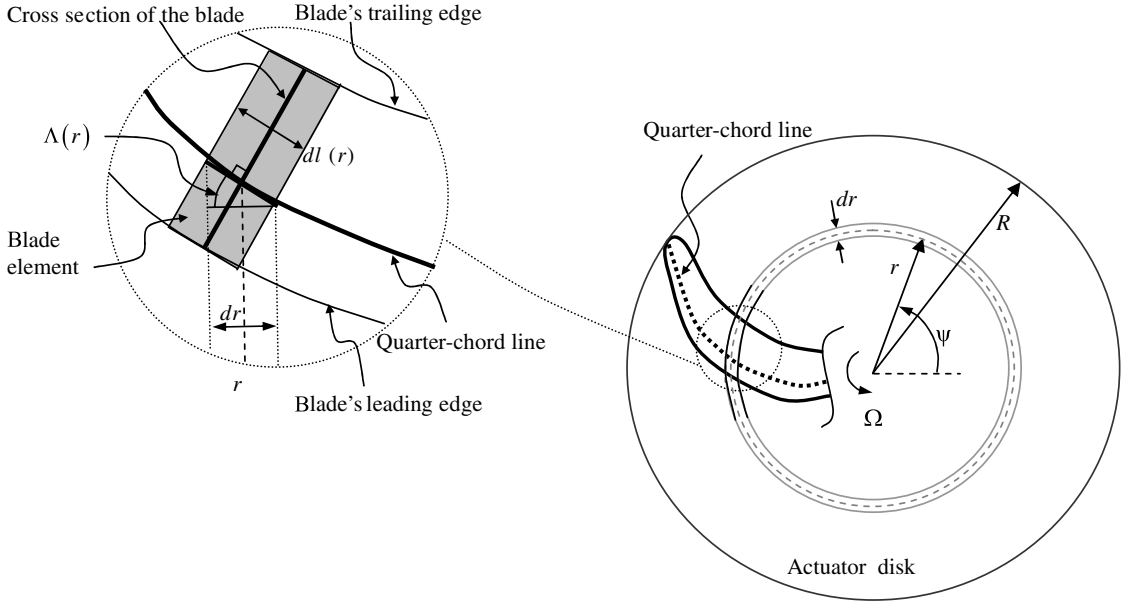

Fig. 1 Actuator disk and a representative blade.

line. In the case of straight blades, the quarter-chord line is a radial line. In the case of curved blades, the quarter-chord line is a curved line, lying in the plane of rotation.

Each point along the quarter-chord line is defined by its radial coordinate r. It should be noted that in the case of curved blades, different points along the quarter-chord line are associated with variations in the azimuth angle (which are functions of r). The radial coordinate of the blade tip R defines the radius of the actuator disk.

Consider now an annulus of the actuator disk (see Fig. 1), which is defined by its radius r and width dr. The outer and inner radii of the annulus are $r + \mathrm{d}r/2$ and $r - \mathrm{d}r/2$, respectively. N_b blade elements are rotating inside this annulus. The length of each element is d$l(r)$, measured along the quarter-chord line, where

$$\mathrm{d}\,l(r) = \frac{\mathrm{d}r}{\cos[\Lambda(r)]} \tag{2}$$

and $\Lambda(r)$ is the local sweep angle, which is positive in the case of forward sweep (in Fig. 1, the sweep angle is negative).

The cross section r has a chord length $c(r)$ and its pitch angle (the angle between the chord line and the plane of rotation) is $\theta(r)$ (see Fig. 2). At time t, the angular location of cross section r of a blade rotating at a constant angular speed Ω is

$$\psi(r, t) = \psi_0(r) + \Omega \cdot t \tag{3}$$

where $\psi_0(r)$ is the angular location of cross section r at $t = 0$.

The flowfield at cross section r, which is located at an azimuth ψ, is shown in Fig. 2. $U(r, \psi)$ is the resultant velocity at the blade cross section and is composed of the incoming flow velocity V, blade rotation speed $\Omega \cdot r$, influences of sweep angle $\Lambda(r)$, and the three components of the induced velocity "seen" by the cross section r at the moment when its azimuth angle is ψ: $w_z(r, \psi)$, $w_\psi(r, \psi)$, and $w_r(r, \psi)$. The last terms are not functions of time because a steady case is considered in which the time-averaged induced velocity at any point (r, ψ) is calculated.

According to the usual blade-element approach, it is assumed that each cross section that is not at a close proximity of the blade tip or root behaves aerodynamically, as with the same cross section in an identical two-dimensional flow. Thus, the two components of the cross-sectional aerodynamic force per unit length, the lift L' [the component perpendicular to $U(r, \psi)$] and the drag D' [the component in the $U(r, \psi)$ direction] are, respectively,

$$L'(r, \psi) = \tfrac{1}{2} \cdot \rho \cdot U^2(r, \psi) \cdot c(r) \cdot C_l[\alpha(r, \psi), M(r, \psi), Re(r, \psi)] \tag{4a}$$

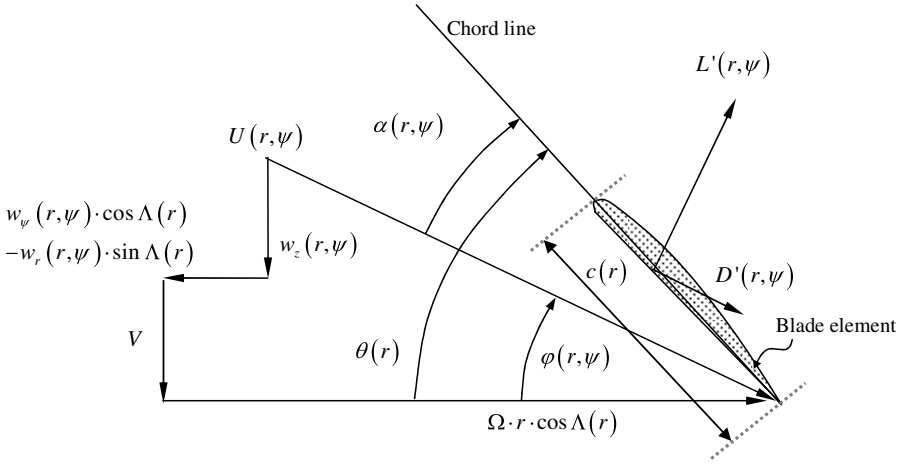

Fig. 2 Cross section of a blade element.

$$D'(r,\psi)=\tfrac{1}{2}\cdot\rho\cdot U^2(r,\psi)\cdot c(r)\cdot C_d[\alpha(r,\psi),M(r,\psi),Re(r,\psi)] \tag{4b}$$

where ρ is the fluid mass density, and C_l and C_d are the two-dimensional cross-sectional lift and drag coefficients, respectively, which are functions of the cross-sectional angle of attack $\alpha(r,\psi)$, Mach number $M(r,\psi)$, and Reynolds number $Re(r,\psi)$.

Near the blade tip or blade root, C_l and C_d should be corrected for three-dimensional effects. This correction includes multiplication of the two-dimensional coefficients by correction factors. These correction factors can include a simple tip loss factor B_{tip}, assuming that the lift becomes zero [25] for sections in which $r > B_{\text{tip}}\cdot R$, or they can be based on more elaborate calculations that take into account the exact shape of the blade tip [26]. Moreover, for curved blades, 3-D effects occur along the entire blade [27]. Nevertheless, for practical cases, these effects are usually small and thus can be neglected. The regular blade-element approach also neglects the influence of spanwise flow components (namely, flow normal to the cross sections). This assumption has been verified by various investigations in the past [28]. Spanwise flow occurs due to the radial induced velocity (even in the case of straight blades) and it intensifies in the case of curved (swept) blades. The present actuator disk model is capable of calculating the radial induced velocity. Thus, if necessary, the influence of a spanwise flow component can be taken into account.

$F_r(r,\psi)$, $F_\psi(r,\psi)$, and $F_z(r,\psi)$ are the radial, circumferential, and axial components, respectively, of the aerodynamic force acting on a unit length of the blade at cross section r at an azimuth angle ψ. Based on the previous derivations (Figs. 1 and 2),

$$F_r(r,\psi)=\{L'(r,\psi)\cdot\sin\varphi(r,\psi)+D'(r,\psi)\cdot\cos\varphi(r,\psi)\}\cdot\sin\Lambda(r) \tag{5a}$$

$$F_\psi(r,\psi)=-\{L'(r,\psi)\cdot\sin\varphi(r,\psi)+D'(r,\psi)\cdot\cos\varphi(r,\psi)\}\cdot\cos\Lambda(r) \tag{5b}$$

$$F_z(r,\psi)=-L'(r,\psi)\cdot\cos\varphi(r,\psi)+D'(r,\psi)\cdot\sin\varphi(r,\psi) \tag{5c}$$

where $\varphi(r,\psi)$ is the local inflow angle, defined in Fig. 2, and the lift per unit length $L'(r,\psi)$ is a result of the pressure difference between both sides of the cross section.

The pressure difference is a function of the chordwise coordinate. The average chordwise pressure difference of cross section r at azimuth angle ψ is denoted as $\Delta p(r,\psi)$; thus,

$$L'(r,\psi)=\Delta p(r,\psi)\cdot\tilde{c}(r) \tag{6}$$

where $\tilde{c}(r)$ is the equivalent chord, which is the projection of the chord on the direction of $U(r,\psi)$: namely,

$$\tilde{c}(r)=c(r)\cdot\cos\alpha \tag{7}$$

The average chordwise pressure on the upper and lower surfaces of that cross section are $p_u(r,\psi)$ and $p_l(r,\psi)$, respectively, where

$$\Delta p(r,\psi)=p_l(r,\psi)-p_u(r,\psi) \tag{8a}$$

$$p_u(r,\psi)=p_\infty+p_0(r,\psi)+\Delta p_u(r,\psi) \tag{8b}$$

$$p_l(r,\psi)=p_\infty+p_0(r,\psi)+\Delta p_l(r,\psi) \tag{8c}$$

and $p_\infty+p_0(r,\psi)$ is the pressure of the incoming undisturbed flow as seen by cross section r at an azimuth angle ψ.

According to Eqs. (8a–8c) and based on cross-sectional aerodynamic characteristics,

$$\Delta p_u(r,\psi)=-k(r,\psi)\cdot\Delta p(r,\psi) \tag{9a}$$

$$\Delta p_l(r,\psi)=[1-k(r,\psi)]\cdot\Delta p(r,\psi) \tag{9b}$$

where $k(r,\psi)$, the pressure ratio factor, is a function of $\alpha(r,\psi)$, $M(r,\psi)$, and $Re(r,\psi)$. According to the linear theory of inviscid flow over a two-dimensional thin cross section, $k(r,\psi)=0.5$ (see Appendix A). The viscid actual value can be obtained from measurements of the pressure over a cross section in a two-dimensional flow at various combinations of angle of attack, Mach number, and Reynolds number (see Appendix A).

In the present axisymmetric and steady case (axial flow and a pitch angle that does not change with ψ), all the cross-sectional parameters do not vary with ψ and are functions of r only. Thus, in what follows, the argument ψ will be dropped from all the preceding defined functions.

The actuator disk approach is based on a time averaging of any variable at any point (r,ψ) of the disk. The time averaging in the present case is obtained by multiplying the time-dependent variables by $N_b\cdot\tilde{c}(r)\cdot\cos\varphi(r)/[2\cdot\pi\cdot r\cdot\cos\Lambda(r)]$.

Thus, based on Eqs. (6–9), the pressure just before the flow enters the actuator disk, $p(r,z=0^-)$, and the pressure immediately after the flow crosses the disk, $p(r,z=0^+)$, are

$$p(r,z=0^-)=p_\infty+p_0(r)-k(r)\cdot L'(r)\cdot\frac{N_b\cdot\cos\varphi(r)}{2\cdot\pi\cdot r\cdot\cos\Lambda(r)} \tag{10a}$$

$$p(r,z=0^+)=p_\infty+p_0(r)+[1-k(r)]\cdot L'(r)\cdot\frac{N_b\cdot\cos\varphi(r)}{2\cdot\pi\cdot r\cdot\cos\Lambda(r)} \tag{10b}$$

$P_r(r,z)$, $P_\psi(r,z)$, and $P_z(r,z)$ are the average radial, circumferential, and axial components of the body force per unit volume acting on the flow while it passes through the actuator disk. After neglecting viscid effects [namely, neglecting the influence of $D'(r)$], using Eqs. (5a–5c), and averaging with respect to time, these components become

$$P_r(r,z)=-\frac{N_b\cdot L'(r)\cdot\sin\varphi(r)\cdot\tan\Lambda(r)}{2\cdot\pi\cdot r}\cdot\delta(z) \tag{11a}$$

$$P_\psi(r,z)=\frac{N_b\cdot L'(r)\cdot\sin\varphi(r)}{2\cdot\pi\cdot r}\cdot\delta(z) \tag{11b}$$

$$P_z(r,z)=\frac{N_b\cdot L'(r)\cdot\cos\varphi(r)}{2\cdot\pi\cdot r}\cdot\delta(z) \tag{11c}$$

where $\delta(z)$ is the Dirac delta function.

After the application of the averaging process, the components of the induced velocity and pressure for the present axisymmetric case become functions of r and z only. At the disk, the induced velocity components are $w_r(r)$, $w_\psi(r)$, and $w_z(r)$.

The axisymmetric, inviscid, and incompressible momentum equations of the flow through the actuator disk are

$$v_r\cdot\frac{\partial v_r}{\partial r}+(V+v_z)\cdot\frac{\partial v_r}{\partial z}-\frac{1}{r}\cdot v_\psi^2=\frac{1}{\rho}\cdot\left(-\frac{\partial p}{\partial r}+P_r\right) \tag{12a}$$

$$v_r\cdot\frac{\partial v_\psi}{\partial r}+(V+v_z)\cdot\frac{\partial v_\psi}{\partial z}+\frac{1}{r}\cdot v_r\cdot v_\psi=\frac{1}{\rho}\cdot P_\psi \tag{12b}$$

$$v_r\cdot\frac{\partial v_z}{\partial r}+(V+v_z)\cdot\frac{\partial v_z}{\partial z}=\frac{1}{\rho}\cdot\left(-\frac{\partial p}{\partial z}+P_z\right) \tag{12c}$$

The continuity equation for this case is

$$\frac{1}{r}\cdot\frac{\partial(r\cdot v_r)}{\partial r}+\frac{\partial v_z}{\partial z}=0 \tag{13}$$

All the variables appearing in Eqs. (12a–12c) and (13) are functions of r and z.

Integration with respect to z of the continuity equation (13) from $z=0^-$ to 0^+ results in

$$v_z(r,z=0^+)-v_z(r,z=0^-)=0 \tag{14}$$

Equation (14) indicates that there is a continuity of the axial velocity through the disk: namely,

$$v_z(r,z=0^+)=v_z(r,z=0^-)=w_z(r) \tag{15}$$

Similar integration across the disk of Eq. (12c) and using Eq. (15) indicates that

$$p(r,z=0^+)-p(r,z=0^-)=\frac{N_b\cdot\cos\varphi(r)\cdot L'(r)}{2\cdot\pi\cdot r\cdot\cos\Lambda(r)} \tag{16}$$

Equation (16) is in agreement with Eqs. (10a) and (10b).

Integration across the disk (with respect to z from $z=0^-$ to 0^+) of Eqs. (12a) and (12b) results in

$$[V+w_z(r)]\cdot[v_r(r,z=0^+)-v_r(r,z=0^-)]=\frac{1}{\rho}\cdot\frac{N_b\cdot\sin\varphi(r)\cdot\tan\Lambda(r)\cdot L'(r)}{2\cdot\pi\cdot r} \tag{17a}$$

$$[V+w_z(r)]\cdot[v_\psi(r,z=0^+)-v_\psi(r,z=0^-)]=\frac{1}{\rho}\cdot\frac{N_b\cdot\sin\varphi(r)\cdot L'(r)}{2\cdot\pi\cdot r} \tag{17b}$$

Equation (17a) indicates that discontinuity in the radial component of the induced velocity may occur only in the case of curved blades or when $[V+w_z(r)]=0$. The last condition may occur only when the freestream velocity is relatively small, such as a helicopter rotor at hovering or a propeller operating at static conditions. On the other hand, only in the case of contrarotating rotors (where the resultant term $N_b\cdot\sin\varphi(r)\cdot L'(r)$ of both rotors becomes zero) or when $[V+w_z(r)]=0$ and thus $\varphi(r)=0$ there may be a continuity in the circumferential induced velocity.

Based on conservation of angular momentum, assuming that a fluid particle does not cross the disk more than one time results in

$$v_\psi(r,z)=0 \quad \text{for } z<0 \tag{18}$$

It is also common to assume

$$w_\psi(r)=\tfrac{1}{2}\cdot[v_\psi(r,z=0^-)+v_\psi(r,z=0^+)]=\tfrac{1}{2}\cdot v_\psi(r,z=0^+) \tag{19a}$$

$$w_r(r)=\tfrac{1}{2}\cdot[v_r(r,z=0^+)+v_r(r,z=0^-)] \tag{19b}$$

B. Wake

The wake starts at the actuator disk plane $z=0^+$ and continues to infinity $z\to+\infty$. As defined in the previous subsection, at $z=0^+$ the components of the induced velocity are $v_r(r,z=0^+)$, $v_\psi(r,z=0^+)$, and $w_z(r)$. The pressure is $p(r,z=0^+)$. In the previous subsection, an annulus of the disk was defined by its outer and inner radii, $r+\mathrm{d}r/2$ and $r-\mathrm{d}r/2$, respectively. The annulus width is $\mathrm{d}r$. The streamlines that pass through the boundaries of this annulus define an annular control volume. The radius of this control volume in the far wake $z\to+\infty$ is r' and its width is $\mathrm{d}r'$, as shown in Fig. 3, where r' is a function of r; thus,

$$r'=r'(r) \tag{20a}$$

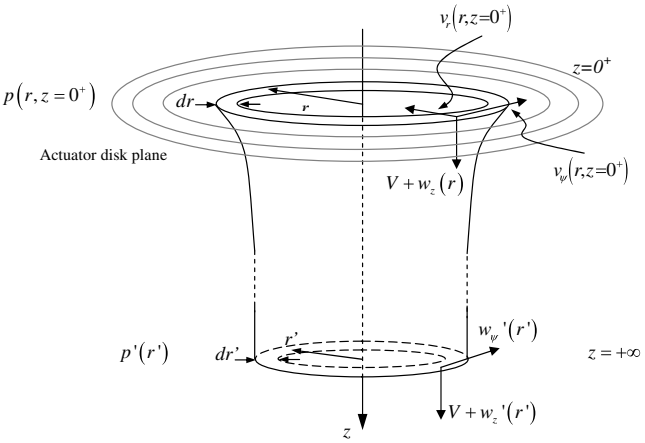

Fig. 3 Control volume of the wake.

$$\mathrm{d}r'=\mathrm{d}r'(r) \tag{20b}$$

The induced velocity components in the far wake are $w_r'(r')$, $w_\psi'(r')$, and $w_z'(r')$. According to the present assumptions, $w_r'(r')=0$.

Because of conservation of mass,

$$[V+w_z(r)]\cdot r\cdot\mathrm{d}r=[V+w_z'(r')]\cdot r'\cdot\mathrm{d}r' \tag{21}$$

Bernoulli's equation along a streamline in the wake results in

$$\frac{\rho}{2}\cdot\{[V+w_z(r)]^2+v_\psi^2(r,z=0^+)+v_r^2(r,z=0^+)\}+p(r,z=0^+)=\frac{\rho}{2}\cdot\{[V+w_z'(r')]^2+w_\psi'^2(r')\}+p'(r') \tag{22}$$

Equation (12a) implies

$$\frac{\mathrm{d}p'(r')}{\mathrm{d}r'}=\rho\cdot\frac{w_\psi'^2(r')}{r'} \tag{23}$$

where

$$p'(r')=p_\infty \quad \text{for } r'\geq r'(R) \tag{24}$$

Conservation of angular momentum and use of Eq. (21) results in

$$w_\psi'(r')\cdot r'=v_\psi(r,z=0^+)\cdot r \tag{25}$$

All the equations of this subsection are identical to the far-wake equations of the general momentum theory.

C. Rest of the Flowfield

Consider the half-space $z<0$. The actuator disk can be looked upon as an apparatus that sucks the fluid from that region and pumps it downstream into the wake. This mechanism can be modeled for the region $z<0$ as a distribution of sinks over the actuator disk. Because the present case is axisymmetric, the sink distribution should also be axisymmetric: namely, a function of r only. The intensity of the sink distribution per unit area of the disk is denoted as $\gamma(r)$.

Moreover, it is clear that the actuator disk will induce an axial velocity through the plane $z=0$, also outside the disk area. Thus, $\gamma(r)$ exists for $0<r<\infty$ (for more details, see the discussion at the end of the present subsection).

Appendix B presents an analysis of the flowfield induced by such a sink distribution. Based on Eqs. (15) and (B9) of Appendix B,

$$\gamma(r)=2\cdot w_z(r) \tag{26}$$

Substitution of Eq. (26) into Eq. (B19) results in the following expression for the radial component of the induced velocity, immediately before the flow crosses the plane $z=0$:

$$v_r(r, z=0^-) = \lim_{\varepsilon\to 0}\left\{-\frac{1}{\pi}\cdot\int_{r_1=0}^{r_1=r-\varepsilon} w_z(r_1)\cdot r_1\cdot[r\cdot A(r,z,r_1) - r_1 \cdot B(r,z,r_1)]\cdot \mathrm{d}r_1 - \frac{1}{\pi}\cdot\int_{r_1=r+\varepsilon}^{r_1\to\infty} w_z(r_1)\cdot r_1\cdot[r\cdot A(r,z,r_1) - r_1 \cdot B(r,z,r_1)]\cdot \mathrm{d}r_1 + \frac{w_z(r)}{\pi\cdot r}\cdot\varepsilon\cdot \ell_n\,\varepsilon\right\} \tag{27}$$

The various parameters appearing in Eq. (27) are defined in Appendix B. As ε approaches zero, the limit of $\varepsilon\cdot\ell_n\,\varepsilon$ becomes zero. Thus, the limit of the two integrals in the last equation is the Cauchy principal value of the entire integral from $r_1 = 0$ to ∞.

Because it is assumed that any fluid particle crosses the actuator disk only once, the Bernoulli equation for a streamline that passes at a point $z = 0^-$ over the disk becomes [use is also made of Eq. (18)]

$$\tfrac{1}{2}\cdot\rho\cdot[2\cdot V\cdot w_z(r) + w_z^2(r) + v_r^2(r, z=0^-)] + p(r, z=0^-) = 0 \tag{28}$$

By using Eq. (27), the value of $v_r(r, z=0^-)$ is also obtained for points outside the disk area. As indicated, because continuity of the flow and pressure across the plane $z = 0$ should exist for $r > R$, it is clear that there is also an axial induced velocity outside the disk, $w_z(r > R)$. A first-order approximation for $w_z(r)$ outside the disk area is discussed in Appendix C.

D. Solution Procedure

The present analysis includes an iterative solution procedure. Each iteration loop includes three stages: 1) finding the flow that passes through the actuator disk, 2) finding the flow in the far wake, and 3) checking convergence and preparing the next iteration if necessary. There may also be an iterative procedure within each stage. In what follows, the three stages will be described.

1. *Stage I*

It is assumed that $p_0(r)$ is known. At the beginning of the first iteration, $p_0(r)$ can be chosen to be equal to zero. There are 11 unknowns associated with this stage:

$$w_r(r),\quad w_\psi(r),\quad w_z(r),\quad v_r(r, z=0^-)$$
$$v_r(r, z=0^+),\quad v_\psi(r, z=0^+),\quad p(r, z=0^-)$$
$$L'(r),\quad \varphi(r),\quad \alpha(r),\quad U(r)$$

Based on the derivations of Secs. II.A and II.C, the following eight equations are used during the solution procedure of this stage: Eqs. (4a), (10a), (17a), (17b), (19a), (19b), (27), and (28).

There are an additional three equations that are obtained from geometric relations presented in Fig. 2:

$$\varphi(r) = \tan^{-1}\left[\frac{V + w_z(r)}{\Omega\cdot r\cdot\cos\Lambda(r) - w_\psi(r)\cdot\cos\Lambda(r) + w_r(r)\cdot\sin\Lambda(r)}\right] \tag{29a}$$

$$U(r) = \sqrt{[V + w_z(r)]^2 + [\Omega\cdot r\cdot\cos\Lambda(r) - w_\psi(r)\cdot\cos\Lambda(r) + w_r(r)\cdot\sin\Lambda(r)]^2} \tag{29b}$$

$$\alpha(r) = \theta(r) - \varphi(r) \tag{29c}$$

Thus, the 11 equations are used to solve for the 11 unknowns. Because of the nonlinear nature of the equations, the solution procedure is iterative. At the beginning of the first iteration, the various components of the induced velocity are assumed to be equal to zero (other initial values can also be used, based on any previous data). Based on the initial data, $\varphi(r)$, $V(r)$, $\alpha(r)$, $L'(r)$, and $p(r, z = 0^-)$ are calculated. Equation (28) is used to calculate $w_z(r)$. The new value of $w_z(r)$ and integration according to Eq. (27) result in the value of $v_r(r, z=0^-)$. Then the values of $v_r(r, z=0^+)$ and $v_\psi(r, z=0^+)$ are calculated according to Eqs. (17a) and (17b). Finally, $w_\psi(r)$ and $w_r(r)$ are obtained by Eqs. (19a) and (19b). The preceding described procedure is repeated until convergence.

It should be noted that the solution procedure includes an additional set of variables: $C_l(r)$, $C_d(r)$, and $k(r)$. These variables are functions of the cross-sectional aerodynamic characteristics and flow conditions: namely, $\alpha(r)$, $M(r)$, and $Re(r)$.

2. *Stage II*

The unknowns associated with this stage are $p(r, z=0^+)$, $r'(r)$, $w'_\psi(r)$, $w'_z(r)$, and $p'(r)$. The five equations that are used to find these unknowns are Eqs. (16), (21–23), and (25). In addition, the condition of Eq. (24) is also applied.

3. *Stage III*

At this stage, the convergence of the entire solution is examined. The convergence criterion is based on conservation of axial momentum. This condition is expressed by the following equation:

$$\int_0^R \Delta p(r)\cdot r\cdot\mathrm{d}r - \int_0^{r'(R)} p'(r')\cdot r'\cdot\mathrm{d}r' = \rho\cdot\int_0^{r'(R)}[V + w'_z(r')]\cdot w'_z(r')\cdot r'\cdot\mathrm{d}r' \tag{30}$$

By using Eq. (21), the last equation can be written as

$$\int_0^R \Delta p_e(r)\cdot r\cdot\mathrm{d}r = \rho\cdot\int_0^{r'(R)}[V + w'_z(r')]\cdot w'_z(r')\cdot r'\cdot\mathrm{d}r' \tag{31a}$$

$$\Delta p_e(r) = \Delta p(r) - p'[r'(r)]\cdot\frac{V + w_z(r)}{V + w'_z[r'(r)]} \tag{31b}$$

where $\Delta p_e(r)$ can be looked upon as an equivalent pressure difference across the disk. Thus, based on Eqs. (8b) and (9a), to satisfy the momentum equation, $p_0(r)$ is chosen as

$$p_0(r) = k(r)\cdot p'[r'(r)]\cdot\frac{V + w_z(r)}{V + w'_z[r'(r)]} \tag{32}$$

The preceding described step [defining $p_0(r)$ by Eq. (32)] still does not assure the conservation of axial momentum. Thus, if necessary, $k(r)$ will be varied by a certain constant factor until Eq. (29) is satisfied (based on a predetermined convergence criterion). If this factor is described by $1 + C$, it simply indicates that Eq. (32) should be replaced by the following equation:

$$p_0(r) = (1 + C)\cdot k(r)\cdot p'[r'(r)]\cdot\frac{V + w_z(r)}{V + w'_z[r'(r)]} - C\cdot k(r)\cdot\Delta p(r) \tag{33}$$

At this stage, the value of $p_0(r)$ according to Eq. (33) is compared with the value of $p_0(r)$ that was used as an input for the first stage. If the difference between both is larger than a predetermined convergence criterion, a new iteration cycle is started.

It should be noted that the solution mainly involves the actuator disk and the rest of the plane $z = 0$. The wake flow is part of the test for convergence of the entire iterative solution, especially the function $p_0(r)$.

The present iterative procedure usually converges fast and it is numerically efficient. Yet the present model, which is simpler and faster than other exact models [13,16,21], does not offer a detailed accurate solution of the entire flowfield as do the exact models. Instead, the present model concentrates on the flow at the disk plane.

III. Results

The results of the new model are compared with results from the literature. The following two cases will be presented and discussed: 1) comparison with test results of propeller in axial flight [29] and 2) comparison with exact analytical results [21].

A. Propeller in Axial Flight

McLemore and Cannon [29] presented test results for the performance of a four-bladed propeller at various angles of attack and various pitch angles. The present comparison will be confined to the case of axial flow and two different pitch angles: $\theta_{0.75} = 30, 40$ deg, where $\theta_{0.75}$ is the pitch angle at the three-quarter-blade's cross section. The blades' cross sections are members of the NACA-16 series. Details on the geometry of the propeller's blades and the test conditions are presented in [29].

The results include the thrust coefficient C_T and the power coefficient C_P as functions of the advance ratio J:

$$C_T = \frac{T}{\rho \cdot n^2 \cdot D^4} \tag{34a}$$

$$C_p = \frac{P}{\rho \cdot n^3 \cdot D^5} \tag{34b}$$

$$J = \frac{V}{n \cdot D} \tag{34c}$$

where T is the propeller's thrust, P is the required power, D is the propeller's diameter, and n is the angular speed given in revolutions per second. The resultant thrust and power are obtained by integration of the aerodynamic loads along the blades.

Thrust and power coefficients are shown in Fig. 4. In this figure, the results of a general momentum theory are also presented. At high advance ratios ($J > 0.8$ for $\theta_{0.75} = 30$ deg and $J > 1.4$ for $\theta_{0.75} = 40$ deg), only small parts of the blade experience stall (see Gur and Rosen [30]), and thus there is good agreement between the calculated results and test results. The results of the present model show a slightly better agreement with the test results than the results of the general momentum model.

The calculations were performed on a 2.4 GHz Pentium-4 desktop PC with 1 GB RAM. On average, the present model required 1 s per each point, whereas the general momentum model was even faster. Prescribed wake calculations were longer by 2 orders of magnitude and free-wake calculations were much longer [28].

More detailed comparisons between the results of the present model and those of the general momentum model are shown in Fig. 5 for the case with $\theta_{0.75} = 30$ deg and $J = 0.8$. It is shown that at the inner part of the disk, the present model gives higher axial induced velocities than the results of the general momentum model. On the other hand, close to the tip, the present model gives lower axial induced velocities, even showing negative values near the rim of the disk. Although the differences in the induced velocities have a very small influence on the loading at the inner part of the disk, they exhibit more significant influence on the aerodynamic loads close to the rim of the disk, with higher loads in the case of the present model (because of smaller axial induced velocities there). These differences near the rim result in the slightly higher thrust coefficients that are shown in Fig. 4.

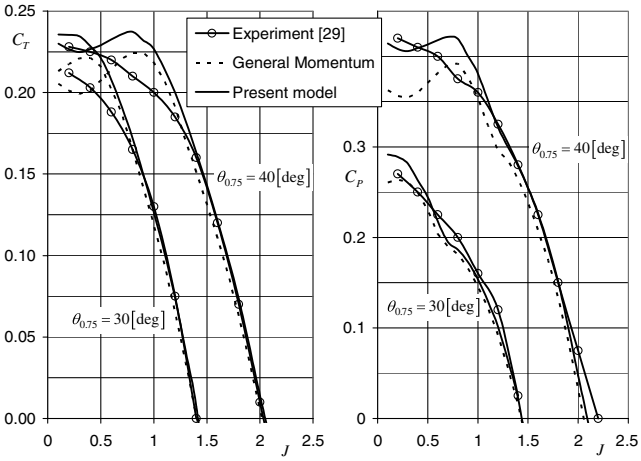

Fig. 4 Four-bladed propeller: comparison between the thrust and power coefficients obtained by the present model, general momentum model, and experimental results of McLemore and Cannon [29].

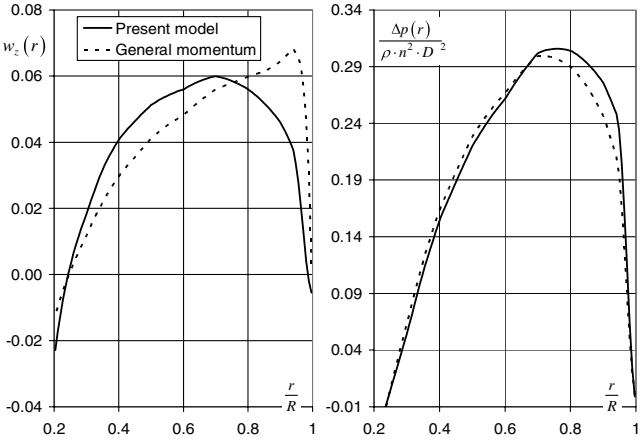

Fig. 5 Four-bladed propeller: comparison between radial distributions of the axial induced velocity and disk loading as obtained by the present model and the general momentum model; $J = 0.8$ and $\theta_{0.75} = 30$ deg.

For low advance ratios, increasing parts of the blades experience stall. There is a problem of accurate modeling of stall in the case of rotating blades [30], resulting in increasing differences between the results of the two models and the test results. Furthermore, there are increasing differences between the results of the present model and those of the general momentum model. It seems that the results of the present new model agree better with the trends of the test results. The new results do not exhibit the relatively large drop in thrust and power coefficients at low advance ratios that are shown by the general momentum model.

B. Comparison with Analytical Results

Conway [21] presented exact results for the flowfield of an actuator disk. He used the following definition for the rotor thrust coefficient C_{th}:

$$C_{\text{th}} = \frac{T}{\frac{1}{2} \cdot \rho \cdot R^2 \cdot V^2} \tag{35}$$

Conway [21] investigated three different loadings, among them a typical rotor loading with slipstream rotation. The loading distribution is shown in Fig. 6. For the case that will be investigated, $C_{\text{th}} = 0.8903$ and $J = 1$.

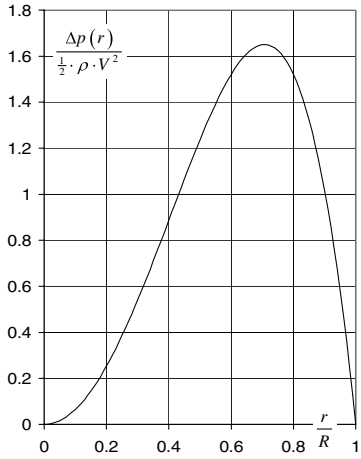

Fig. 6 Aerodynamic load distribution used for comparison with the results of Conway [21].

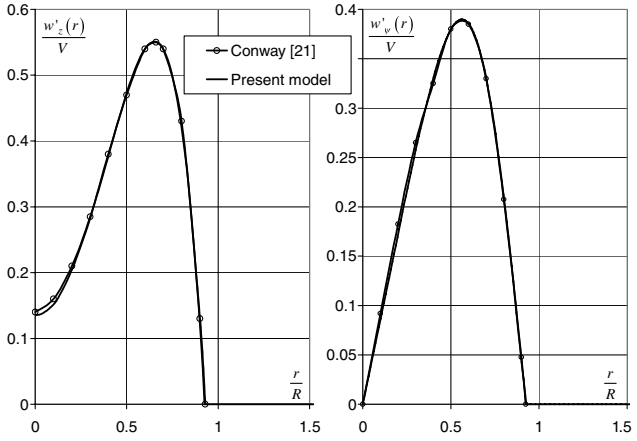

Fig. 8 Comparison with the results of Conway [21]: axial and circumferential induced velocities at the far wake, $z \to \infty$.

Results will be shown at two regions: the disk plane $z = 0$ and the far wake $z \to \infty$. For each of these regions, the velocity components according to the model of Conway [21] was obtained from the figures of [21], and thus certain inaccuracies may exist. In all cases, the present new model uses the theoretical ideal value $k = 0.5$.

The calculations converged after 5 iteration cycles, yielding $C = -0.04$ and showing that the magnitude of $p_0(r)$ required for obtaining conservation of axial momentum is relatively small. A significant contribution to $p_0(r)$ comes from the wake rotation. Conway's [21] exact model was also implemented on a 2.4 GHz Pentium-4 desktop PC with 1 GB RAM. The required computing time was at least 3 orders of magnitude larger than for the present model.

The axial, radial, and circumferential induced velocities at the disk plane are shown in Fig. 7. Three kinds of results of the present model are shown: 1) a complete converged model, 2) a model in which C in Eq. (33) is taken equal to zero, and 3) a model in which $p'[r'(r)]$ in Eq. (33) is taken equal to zero.

In case 2, conservation of axial momentum does not necessarily exist. In case 3, the influence of the pressure in the far wake, on the velocities that are induced at the disk plane, is neglected.

In the case of the axial and radial induced velocities (Fig. 7), the agreement between the results of Conway [21] and the results of cases 1 and 2 is very good. As expected, the results of case 3 differ from the other results at the inner part of the disk $0 < r < 0.6 \cdot R$. It is interesting to note that the present model and Conway's results show negative values of the axial induced velocities near the disk rim. In the case of the radial induced velocity, there is good agreement between the results of Conway and the present results, except for the results of case 3, which exhibit significant differences in the inner part of the disk. The agreement between the results for the circumferential induced velocities (Fig. 7) for all the models is excellent.

Figure 8 shows excellent agreement between the results of Conway [21] and the results of the present model concerning the axial and circumferential components of the induced velocity in the far wake $z \to \infty$. The results indicate that the diameter of the far wake [namely, $r'(R)$] is practically identical for both models.

IV. Conclusions

A new actuator disk model is presented. The derivation of the model for the case of an axial axisymmetric flow is discussed. The entire flowfield is divided into three regions: the actuator disk, the wake, and the rest of the flowfield. The actuator disk is analyzed by using a common blade-element approach. Swept blades as well as straight blades are considered. It is assumed that, at any point of the disk, the pressure difference between both sides of the disk is a result of time averaging of the pressure difference between both sides of the blade elements that pass through that point. The pressure on both sides of the airfoil is obtained from either theoretical derivations or from test results of a two-dimensional flow over the same airfoil. These data are a function of angle of attack, Mach number, and Reynolds number. The relations between the flow characteristics before the flow crosses the disk and just after it passes it are obtained by examining the appropriate momentum and continuity equations. The equations associated with the wake are identical to the wake equations of the general momentum theory.

The analysis of the rest of the flowfield includes the calculation of the induced velocities just before the flow crosses the disk. To calculate those induced velocities, the influence of the disk on the

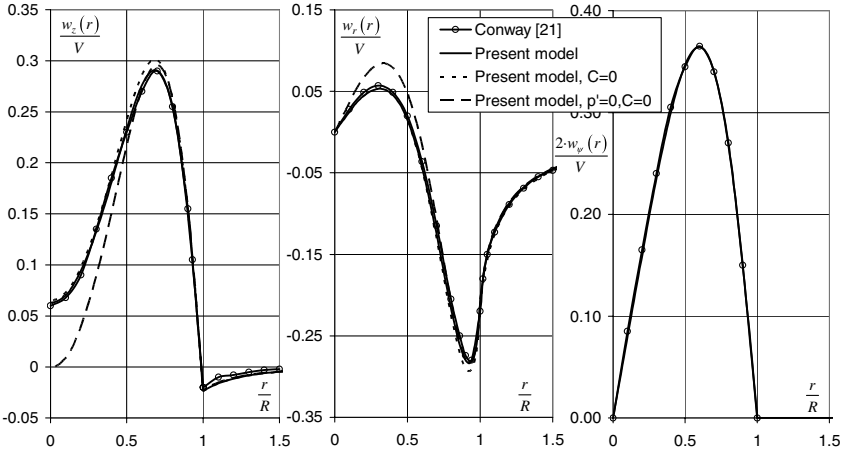

Fig. 7 Comparison with the results of Conway [21]: axial, radial, and circumferential induced velocities at the disk plane.

flow is modeled by an axisymmetric distribution of sinks over the disk plane. The intensity of the sinks is directly proportional to the magnitude of the axial induced velocity at that point. Integral relation yields the value of the radial component of the induced velocity at any point of the disk plane. The calculation of this integral involves singularity problems, which are solved by analytical derivations at the vicinity of the singular points.

The capability of calculating the radial induced velocity is important. It has been shown by Rosen [31] that this velocity component has a very important influence on the flowfield of maneuvering rotors. Thus, accurate calculations of the radial induced velocity may be important for efficient and accurate calculations of the aerodynamics of maneuvering helicopters.

A first-order approximation is used for calculating the axial induced velocities at the disk plane, at radial distances larger than the disk radius. The solution of the nonlinear equations involves an iterative procedure. This procedure usually converges fast. The convergence criterion of the entire iterative procedure is based on conservation of the integral axial momentum.

Comparisons of the results of the present model with the test results of McLemore and Cannon [29] for a four-bladed propeller in axial flow show good agreement at high advance ratios. At low advance ratios, the present model and the general momentum model fail to predict the experimental results, probably because increasing parts of the blades experience stall.

Comparisons of the results of the present model with those of the exact model of Conway [21] show very good agreement. It should be noted that Conway's model is much more complicated and requires much longer computing time. It is also important to note that the negative values of the induced velocity near the rim of the actuator disk agree very well with the upwash obtained by Conway. The general momentum theory is not capable of predicting this upwash. There is also very good agreement between the radial induced velocity as calculated by Conway and the present results, indicating that the modeling of the disk as a distribution of sinks is an appropriate representation.

The present actuator disk model is an efficient model that gives high-quality results when compared with more complex models and test results. It is suitable for applications requiring efficient simple models, such as simulation or conceptual design. One of the major advantages of the present model is that it can be extended to the case of inclined flow, in which such simple models are not available.

Appendix A: Pressure Ratio Factor $k(r)$

The pressure ratio factor $k(r)$ is defined by Eqs. (9a) and (9b) and gives the ratio between the contribution of the upper and the lower surfaces of an airfoil to the pressure difference between those two surfaces.

Consider a two-dimensional flow about an airfoil. The pressure of the undisturbed flow is p_∞, and x is a coordinate along the chord, where $x = 0$ at the leading edge and $x = c$ at the trailing edge. The pressure on the upper surface is $p_\infty + \Delta p_u(x/c)$, and the pressure on the lower surface is $p_\infty + \Delta p_l(x/c)$.

The lift per unit length of the airfoil is L' and it is the result of a contribution of the upper surface ΔL_u and lower surface ΔL_l; thus,

$$L' = \Delta L_u + \Delta L_l \tag{A1}$$

The terms in Eq. (A1) can be written as functions of the upper and lower pressures:

$$\Delta L_u = -c \cdot \int_0^1 \left[\Delta p_u\left(\frac{x}{c}\right) - \Delta p_{u0}\left(\frac{x}{c}\right) \right] \cdot \mathrm{d}\left(\frac{x}{c}\right) \tag{A2a}$$

$$\Delta L_l = c \cdot \int_0^1 \left[\Delta p_l\left(\frac{x}{c}\right) - \Delta p_{l0}\left(\frac{x}{c}\right) \right] \cdot \mathrm{d}\left(\frac{x}{c}\right) \tag{A2b}$$

where $\Delta p_{u0}(x/c)$ and $\Delta p_{l0}(x/c)$ are the values of $\Delta p_u(x/c)$ and $\Delta p_l(x/c)$, respectively, for zero lift. According to Eqs. (9a) and (9b), k is defined as follows:

$$\Delta L_u = k \cdot L' \tag{A3a}$$

$$\Delta L_l = (1 - k) \cdot L' \tag{A3b}$$

Thus,

$$k = \frac{\Delta L_u}{L'} = 1 - \frac{\Delta L_l}{L'} \tag{A4}$$

where k is a function of the flow conditions; namely, the section angle of attack α, freestream Mach number M, and Reynolds number Re.

It is convenient to replace the pressure by the pressure coefficient: namely,

$$\tilde{C}_{Pu}\left(\frac{x}{c}\right) = \frac{\Delta p_u(x/c)}{\frac{1}{2} \cdot \rho \cdot V^2} \tag{A5a}$$

$$\tilde{C}_{Pl}\left(\frac{x}{c}\right) = \frac{\Delta p_l(x/c)}{\frac{1}{2} \cdot \rho \cdot V^2} \tag{A5b}$$

where ρ is the fluid mass density and V is the freestream velocity. In the same manner, $\tilde{C}_{Pu0}(x/c)$ and $\tilde{C}_{Pl0}(x/c)$ are defined based on $\Delta P_{u0}(x/c)$ and $\Delta P_{l0}(x/c)$, respectively.

Substitution of Eqs. (A5a) and (A5b) into Eqs. (A2a) and (A2b) and then into Eq. (A4) results in

$$k = \frac{-\int_0^1 [\tilde{C}_{Pu}(x/c) - \tilde{C}_{Pu0}(x/c)] \cdot \mathrm{d}(x/c)}{\int_0^1 [\tilde{C}_{Pl}(x/c) - \tilde{C}_{Pu}(x/c)] \cdot \mathrm{d}(x/c)} \tag{A6}$$

For the simple case of an incompressible ideal two-dimensional flow over a flat plate, the pressure coefficients are [32]

$$\tilde{C}_{Pu}(\xi) = -2 \cdot \alpha \cdot \tan\frac{\xi}{2} \tag{A7a}$$

$$\tilde{C}_{Pl}(\xi) = 2 \cdot \alpha \cdot \tan\frac{\xi}{2} \tag{A7b}$$

$$\tilde{C}_{Pu0}(\xi) = 0 \tag{A7c}$$

$$\tilde{C}_{Pl0}(\xi) = 0 \tag{A7d}$$

where ξ is defined by

$$\frac{x}{c} = \frac{1 + \cos\xi}{2} \qquad 0 < \xi < \pi \tag{A8}$$

Substituting Eqs. (A7a–A7d) into Eq. (A6) results in $k = 0.5$.

In Fig. A1, the experimental value of k for a NACA-0012 airfoil is presented based on the results of Gregory and O'Reilly [33]. In Fig. A2, similar results for a NACA-64A006 airfoil are presented based on the results of McCullough and Gault [34]. The results for the two airfoils indicate that at low values of the lift coefficient, the value of k is somewhat higher than the theoretical value of 0.5. As the angle of attack increases and approaches stall, the value of k increases. The increase in k is more pronounced in the case of NACA 64A006.

Appendix B: Induced Velocity due to a Planar Axisymmetric Distribution of Sinks

A polar system of coordinates (r, ψ, z) is used. There is an axisymmetric distribution of sinks at the plane $z = 0$. The intensity of the sinks' distribution per unit area of the plane is $\gamma(r)$. The field of the induced velocities is symmetric about the plane $z = 0$ and axisymmetric about z.

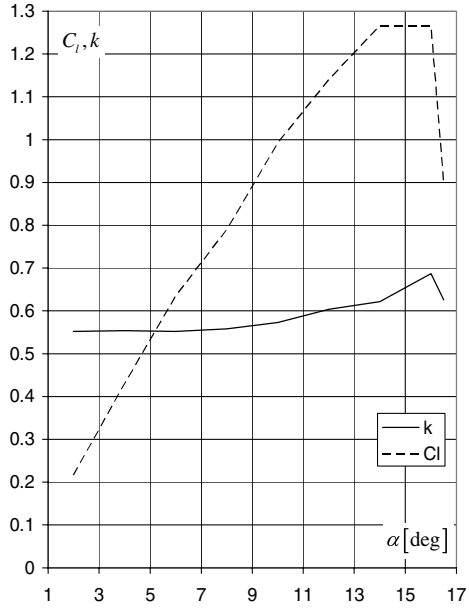

Fig. A1 Lift coefficient and value of k for a NACA-0012 airfoil, as a function of the angle of attack; $M = 0.16$ and $Re = 2.88 \times 10^6$ [33].

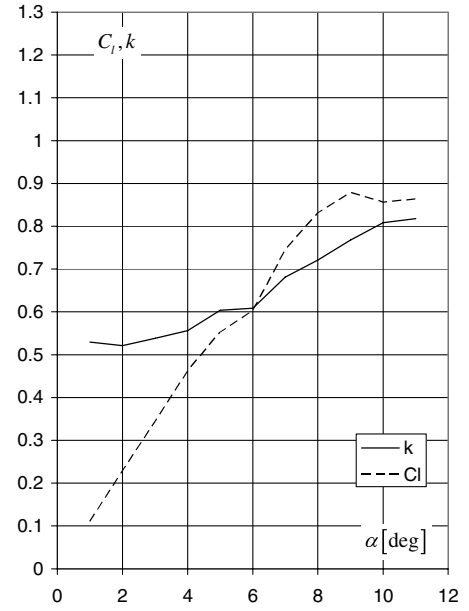

Fig. A2 Lift coefficient and value of k for a NACA-64A006 airfoil, as a function of the angle of attack; $M = 0.17$ and $Re = 5.8 \times 10^6$ [34].

The radial and axial components of the induced velocities are $u_r(r, z)$ and $u_z(r, z)$, respectively:

$$u_z(r,z) = -\frac{z}{2\cdot\pi}\cdot\int_{r_1=0}^{r_1\to\infty}\gamma(r_1)\cdot r_1\cdot A(r,z,r_1)\cdot \mathrm{d}r_1 \tag{B1a}$$

$$u_z(r,z) = -\frac{1}{2\cdot\pi}\cdot\int_{r_1=0}^{r_1\to\infty}\gamma(r_1)\cdot r_1\cdot[r\cdot A(r,z,r_1) - r_1 \cdot B(r,z,r_1)]\cdot \mathrm{d}r_1 \tag{B1b}$$

where $A(r, z, r_1)$ and $B(r, z, r_1)$ are

$$A(r,z,r_1) = \int_{\psi_1=0}^{\psi_1=\pi}\frac{\mathrm{d}\psi_1}{(r^2 + r_1^2 - 2\cdot r\cdot r_1\cdot\cos\psi_1 + z^2)^{\frac{3}{2}}} \tag{B2a}$$

$$B(r,z,r_1) = \int_{\psi_1=0}^{\psi_1=\pi}\frac{\cos\psi_1\cdot\mathrm{d}\psi_1}{(r^2 + r_1^2 - 2\cdot r\cdot r_1\cdot\cos\psi_1 + z^2)^{\frac{3}{2}}} \tag{B2b}$$

Integration of the last two equations [35] results in

$$A(r,z,r_1) = \frac{2}{[(r-r_1)^2 + z^2]\cdot\sqrt{(r+r_1)^2 + z^2}}\cdot E(\kappa) \tag{B3a}$$

$$B(r,z,r_1) = \frac{r^2 + r_1^2 + z^2}{r\cdot r_1[(r-r_1)^2 + z^2]\cdot\sqrt{(r+r_1)^2 + z^2}} \cdot E(\kappa) - \frac{1}{r\cdot r_1\cdot\sqrt{(r+r_1)^2 + z^2}}\cdot K(\kappa) \tag{B3b}$$

where

$$\kappa = 2\cdot\sqrt{\frac{r\cdot r_1}{(r+r_1)^2 + z^2}} \tag{B4}$$

and $K(\kappa)$ and $E(\kappa)$ are complete elliptic integrals of the first kind and the second kind, respectively.

Equations (B3a) and (B3b) are substituted into Eqs. (B1a) and (B1b) and solved numerically. The difficulty of the integration involves a singularity for the case $z \to 0$ and $r_1 \to r$. This singularity will be dealt with in what follows. Because of the symmetry about the $z = 0$ plane, the derivation will be continued for the case $z < 0$.

According to Eq. (B1a), because the integral is multiplied by z, the contribution to $u_z(r, 0^-)$ is confined to the neighborhood of r: namely, $r_1 \to r$; thus,

$$u_z(r,0^-) = \lim_{z\to 0^-}\left[-\frac{z}{2\cdot\pi}\cdot\int_{r_1=r-\varepsilon}^{r_1=r+\varepsilon}\gamma(r_1)\cdot r_1\cdot A(r,z,r_1)\cdot \mathrm{d}r_1\right] \tag{B5}$$

where $0 < \varepsilon \ll 1$.

The integral of (B5) is solved by using the following transformation:

$$t = r_1 - r, \qquad \mathrm{d}t = \mathrm{d}r_1 \tag{B6}$$

The elliptic integral of the second kind is replaced by the first two terms of its series expansion [35]:

$$E(\kappa) \cong 1 - \frac{(\bar{\kappa})^2}{2}\cdot\ell_n(\bar{\kappa}) \tag{B7}$$

where $\bar{\kappa}$ is

$$\bar{\kappa} = \sqrt{1-\kappa^2} \tag{B8}$$

Substituting Eqs. (B6) and (B7) into Eq. (B5) results in

$$u_z(r,0^-) = \lim_{\substack{z\to 0^-\\ \varepsilon\to 0}}\left[-\frac{z}{2\cdot r\cdot\pi} \cdot\int_{t=-\varepsilon}^{t=\varepsilon}\frac{\gamma(r)\cdot r\cdot E(1) + O(t)}{t^2 + z^2}\cdot \mathrm{d}t\right] = \frac{\gamma(r)}{2} \tag{B9}$$

The last result is, in a way, standard and can be obtained directly by applying basic rules of fluid dynamics. It is included here for completeness of the derivation.

The radial component of the induced velocity for $z \to 0^-$, $u_r(r, 0^-)$, becomes

$$u_r(r,0^-) = -\lim_{\varepsilon\to 0}\left\{\frac{1}{2\cdot\pi}\cdot\int_{r_1=0}^{r_1=r-\varepsilon}\gamma(r_1)\cdot r_1 \cdot[r\cdot A(r,0,r_1) - r_1\cdot B(r,0,r_1)]\cdot \mathrm{d}r_1\right\} - \lim_{\varepsilon\to 0}\left\{\frac{1}{2\cdot\pi}\cdot\int_{r_1=r+\varepsilon}^{r_1\to\infty}\gamma(r_1)\cdot r_1 \cdot[r\cdot A(r,0,r_1) - r_1\cdot B(r,0,r_1)]\cdot \mathrm{d}r_1\right\} + I(r,\varepsilon) \tag{B10}$$

The singularity appears in the integral $I(r,\varepsilon)$:

$$I(r,\varepsilon) = -\frac{1}{2\cdot\pi}\cdot\lim_{\substack{z\to 0^-\\ \varepsilon\to 0}}\left\{\int_{r_1=r-\varepsilon}^{r_1=r+\varepsilon}\gamma(r_1) \cdot r_1\cdot[r\cdot A(r,z,r_1) - r_1\cdot B(r,z,r_1)]\cdot \mathrm{d}r_1\right\} \tag{B11}$$

Substituting Eq. (B6) into Eq. (B11) leads to the following expression:

$$I(r,\varepsilon) = \lim_{\substack{z\to 0^-\\ \varepsilon\to 0}}\frac{1}{\pi}\cdot\int_{t=-\varepsilon}^{t=\varepsilon} G(r,t,z)\cdot E[\kappa(r,t,z)]\cdot \mathrm{d}t - \lim_{\substack{z\to 0^-\\ \varepsilon\to 0}}\frac{1}{2\cdot\pi\cdot r} \cdot\int_{t=-\varepsilon}^{t=\varepsilon} H(r,t,z)\cdot\{K[\kappa(r,t,z)] - E[\kappa(r,t,z)]\}\cdot \mathrm{d}t \tag{B12}$$

where

$$\kappa(r,t,z) = 2\cdot\sqrt{\frac{r^2 + r\cdot t}{4\cdot r^2 + 4\cdot r\cdot t + t^2 + z^2}} \tag{B13a}$$

$$G(r,t,z) = \frac{\gamma(r+t)\cdot(r+t)\cdot t}{(t^2+z^2)\cdot\sqrt{4\cdot r^2 + 4\cdot r\cdot t + t^2 + z^2}} \tag{B13b}$$

$$H(r,t,z) = \frac{\gamma(r+t)\cdot(r+t)}{\sqrt{4\cdot r^2 + 4\cdot r\cdot t + t^2 + z^2}} \tag{B13c}$$

A Taylor expansion of $G(r,t,z)$ and $H(r,t,z)$, as defined by Eqs. (B13b) and (B13c), then neglecting high orders of t, leads to the following expressions:

$$G(r,t,z) \cong \frac{\gamma(r)}{2}\cdot\frac{t}{t^2+z^2} + \left[\frac{1}{4}\cdot\frac{\gamma(r)}{r} + \frac{1}{2}\cdot\frac{\mathrm{d}\gamma}{\mathrm{d}r}(r)\right]\cdot\frac{t^2}{t^2+z^2} \tag{B14a}$$

$$H(r,t,z) \cong \frac{\gamma(r)}{2} + \left[\frac{1}{4}\cdot\frac{\gamma(r)}{r} + \frac{1}{2}\cdot\frac{\mathrm{d}\gamma}{\mathrm{d}r}(r)\right]\cdot t \tag{B14b}$$

A series expansion of the complete elliptic integral of the first kind leads to the following approximation [35]:

$$K(\kappa) \cong \ell_n 4 - \ell_n(\bar{\kappa}) \tag{B15}$$

Using Eqs. (B7), (B8), (B13a), and (B15) results in the following approximations for the complete elliptic integrals of the first and second kinds for $z\to 0^-$ and $r_1\to r$:

$$K(r,t,z) \cong \ell_n(8\cdot r) - \tfrac{1}{2}\ell_n(t^2+z^2) \tag{B16a}$$

$$E(r,t,z) \cong 1 - \frac{t^2+z^2}{16\cdot r^2}\cdot\ell_n(t^2+z^2) \tag{B16b}$$

Substitution of Eqs. (B14a) and (B14b) into Eq. (B12) results in

$$I(r,\varepsilon) = \lim_{\substack{z\to 0^-\\ \varepsilon\to 0}}\left[\frac{1}{4}\cdot\frac{\gamma(r)}{r} + \frac{1}{2}\cdot\frac{\mathrm{d}\gamma}{\mathrm{d}r}(r)\right]\cdot\frac{1}{\pi}\cdot\int_{t=-\varepsilon}^{t=\varepsilon}\left[\frac{t^2}{t^2+z^2} - \frac{t^2}{16\cdot r^2}\cdot\ell_n(t^2+z^2)\right]\cdot\mathrm{d}t - \lim_{\substack{z\to 0^-\\ \varepsilon\to 0}}\frac{\gamma(r)}{4\cdot\pi\cdot r} \cdot\int_{t=-\varepsilon}^{t=\varepsilon}\left\{[\ell_n(8\cdot r) - 1] - \frac{1}{2}\cdot\ell_n(t^2+z^2)\right\}\cdot\mathrm{d}t \tag{B17}$$

Carrying out the integrations of the last equation and neglecting higher-order terms in ε, leads to the following approximation for $I(r,\varepsilon)$:

$$I(r,\varepsilon) \cong \frac{\varepsilon}{2\cdot\pi\cdot r}\cdot\left\{\gamma(r)\cdot[\ell_n\,\varepsilon + 1 - \ell_n(8\cdot r)] + 2\cdot\frac{\mathrm{d}\gamma}{\mathrm{d}r}(r)\cdot r\right\} \tag{B18}$$

If ε is small enough, then only the term $[\gamma(r)\cdot\ell_n\,\varepsilon]$ inside the large brackets is retained while neglecting the other much smaller terms. Thus, the final expression of the radial component of the induced velocity for $z = 0^-$, $u_r(r, z=0^-)$, becomes

$$u_r(r,z=0^-) = \lim_{\varepsilon\to 0}\left\{-\frac{1}{2\cdot\pi}\cdot\int_{r_1=0}^{r_1=r-\varepsilon}\gamma(r_1)\cdot r_1 \cdot[r\cdot A(r,z,r_1) - r_1\cdot B(r,z,r_1)]\cdot\mathrm{d}r_1 - \frac{1}{2\cdot\pi}\cdot\int_{r_1=r+\varepsilon}^{r_1\to\infty}\gamma(r_1) \cdot r_1\cdot[r\cdot A(r,z,r_1) - r_1\cdot B(r,z,r_1)]\cdot\mathrm{d}r_1 + \frac{\gamma(r)}{2\cdot\pi\cdot r}\cdot\varepsilon\cdot\ell_n\,\varepsilon\right\} \tag{B19}$$

The procedure of calculating $u_r(r, z=0^-)$ is as follows: An initial value of ε is defined and $u_r(r, z=0^-)$ is calculated according to Eq. (B19), in which numerical integration is used to find the values of the first two integrals. Then ε is reduced and $u_r(r, z=0^-)$ is calculated again. These calculations are repeated until predetermined convergence criteria are met. This procedure is very efficient.

It is worth pointing out that as ε approaches zero, $\varepsilon\cdot\ell_n\,\varepsilon$ approaches zero too, and the expression becomes a Cauchy principal value integral.

Appendix C: Approximation for $w_z(r)$ Outside the disk

The total volumetric flow rate through the disk $0 \le r \le R$ is Q. For points far enough from the disk (and not located near the wake), the induced velocity components are very close to those induced by a sink at the origin of intensity Q: namely,

$$v_r(r,z) \cong -\frac{Q}{4\cdot\pi}\cdot\frac{r}{(r^2+z^2)^{3/2}} \tag{C1a}$$

$$v_z(r,z) \cong -\frac{Q}{4\cdot\pi}\cdot\frac{z}{(r^2+z^2)^{3/2}} \tag{C1b}$$

For the case $z \ll r$ and $r > R$, it is possible to replace Eqs. (C1a) and (C1b) by series that converge rapidly:

$$v_r(r,z) \cong -\frac{Q}{4\cdot\pi}\cdot\left[\frac{1}{r^2} - \frac{3}{2}\cdot\frac{z^2}{r^4} + \frac{15}{8}\cdot\frac{z^4}{r^6}\cdots\right] \tag{C2a}$$

$$v_z(r,z) \cong -\frac{Q}{4\cdot\pi}\cdot\left[\frac{z}{r^3} - \frac{3}{2}\cdot\frac{z^3}{r^5} + \frac{15}{8}\cdot\frac{z^5}{r^7}\cdots\right] \tag{C2b}$$

The purpose now is to change Eqs. (C2a) and (C2b) in such a manner that they will describe the flowfield near the edge of the disk, but for large enough values of r ($r \gg R$) and very small values of z, they will converge to expressions (C2a) and (C2b). Using a first-order approximation, the expression for $v_z(r,z)$ becomes

$$v_z(r,z) \cong \frac{w_z(R)\cdot R^4}{r^4} - \frac{Q}{4\cdot\pi}\cdot\frac{z}{(r^2+z^2)^{3/2}} \quad \text{for } r \geq R \qquad \text{(C3)}$$

The last expression converges to Eq. (C2b) for large enough values of r. At the other end, it results in a continuity in the value of $v_z(r,z)$ for $r = R$ and $z = 0$.

Acknowledgments

The authors would like to thank Jan Dostal, Vyzkumny a Zkusební Letecky Ustav—Centrum Leteckeho a Kosmickeho Vyzkumu (VZLU-CLKV), Prague, for his thorough reading of the manuscript and useful comments. They also would like to thank the reviewers of this paper for their important and helpful comments.

References

[1] Rankine, W. J. M., and Froude, W. M., "On the Mechanical Principles of the Action of Propellers," *Transactions of the Institution of Naval Architects*, Vol. 6, Apr. 1865, pp. 13–39.

[2] Horlock, J. H., *Actuator Disk Theory*, McGraw–Hill, New York, 1978.

[3] Glauert, H., "Airplane Propellers" *Aerodynamic Theory*, Vol. 4, edited by L. Division and F. W. Durand, 3rd ed., Dover, New York, 1963.

[4] Sharpe, D. J., "A General Momentum Theory Applied to an Energy-Extracting Actuator Disk," *Wind Energy Technology*, Vol. 7, No. 3, July 2004, pp. 177–188. doi:10.1002/we.118

[5] Thoma, D., "Grundsatzliches zur Einfachen Strahltheorie der Schraube," *Zeitschrift für Flugtechnik und Motorluftschiffahrt*, Vol. 16, 1925, pp. 206–208.

[6] Goorjian, P. M., "An Invalid Equation in the General Momentum Theory of the Actuator Disk," *AIAA Journal*, Vol. 10, No. 4, Apr. 1972, pp. 543–544. doi:10.2514/3.50146

[7] Rauh, A., and Seelert, W., "The Betz Optimum Efficiency for Windmills," *Applied Energy*, Vol. 17, No. 1, 1984, pp. 15–23. doi:10.1016/0306-2619(84)90037-0

[8] Van Kuik, G. A. M., "On the Limitations of Froude's Actuator Disk Concept," Ph.D. Thesis, Technical Univ. of Eindhoven, Eindhoven, The Netherlands, 1991.

[9] Van Kuik, G. A. M., "On the Revision of the Actuator Disk Momentum Theory," *Wind Engineering*, Vol. 15, No. 5, 1991, pp. 276–289.

[10] Van Kuik, G. A. M., "An Inconsistency in the Actuator Disk Momentum Theory," *Wind Energy Technology*, Vol. 7, No. 1, 2003, pp. 9–19.

[11] Spalart, P. R., "On the Simple Actuator Disk," *Journal of Fluid Mechanics*, Vol. 494, 2003, pp. 399–405. doi:10.1017/S0022112003006128

[12] Bragg, S. L., and Hawthorne, W. R., "Some Exact Solutions of the Flow Through Annular Cascade Actuator Disks," *Journal of the Aeronautical Sciences*, Vol. 17, 1950, pp. 243–249.

[13] Wu, T. Y., "Flow Through a Heavily Loaded Actuator Disk," *Schiffstechnik*, Vol. 9, No. 47, 1962, pp. 134–138.

[14] Hough, G. R., and Ordway, D. E., "The Generalized Actuator Disk," *Developments in Theoretical and Applied Mechanics*, Vol. 2, Pergamon, Toronto, 1964, pp. 317–336.

[15] Greenberg, M. D., and Kaskel, A. L., "Inviscid Flowfield Induced by a Rotor in Ground Effect," NASA CR-1027, May 1968.

[16] Greenberg, M. D., and Powers, S. R., "Nonlinear Actuator Disk Theory and Flowfield Calculations Including Nonuniform Loading," NASA CR-1672, 1970.

[17] Greenberg, M. D., "Nonlinear Actuator Disk Theory," *Zeitschrift für Flugwissenschaften*, Vol. 20, No. 3, 1972, pp. 9–98.

[18] Schmidt, G. H., and Sparenberg, J. A., "On the Edge Singularity of an Actuator Disk with Large Constant Normal Load," *Journal of Ship Research*, Vol. 21, No. 2, 1977, pp. 125–131.

[19] Van der Spek, A. M., "Linear and Nonlinear Theories of Flow Through an Actuator Disk," Dept. of Physics, Technical Univ. of Eindhoven, Rept. R-803-A, Eindhoven, The Netherlands, 1986.

[20] Conway, J. T., "Analytical Solutions for the Actuator Disk with Variable Radial Distribution of Load," *Journal of Fluid Mechanics*, Vol. 297, 1995, pp. 327–355. doi:10.1017/S0022112095003120

[21] Conway, J. T., "Exact Actuator Disk Solutions for Nonuniform Heavy Loading and Slipstream Contraction," *Journal of Fluid Mechanics*, Vol. 365, 1998, pp. 235–267. doi:10.1017/S0022112098001372

[22] Pitt, D. M., and Peters, D. A., "Theoretical Prediction of Dynamic-Inflow Derivatives," *Vertica*, Vol. 5, No. 1, Mar. 1981, pp. 21–34.

[23] Morillo, J. A., and Peters, D. A., "Velocity Field Above a Rotor Disk by a New Dynamic Inflow Model," *Journal of Aircraft*, Vol. 39, No. 5, 2002, pp. 731–738.

[24] Peters, D. A., Morillo, J. A., and Nelson, A. M., "New Developments in Dynamic Wake Modeling for Dynamics Applications," *Journal of the American Helicopter Society*, Vol. 48, No. 2, 2003, pp. 120–127.

[25] Johnson, W., *Helicopter Theory*, Princeton Univ. Press, Princeton, NJ, 1980.

[26] Isser, A., and Rosen, A., "Applying the Lifting Surface Method to the Blade Tip of a Hovering Helicopter," *Computers and Mathematics with Applications*, Vol. 17, No. 11, 1989, pp. 1455–1466. doi:10.1016/0898-1221(89)90078-3

[27] Rosen, A., and Rand, O., "A Model of a Curved Helicopter Blade in Forward Flight," *Vertica*, Vol. 11, No. 1/2, 1987, pp. 211–231.

[28] Gur, O., and Rosen, A., "Comparison Between Blade-Element Models of Propellers," *48th Israel Annual Conference on Aerospace Sciences* [CD-ROM], Faculty of Aerospace Engineering, Technion—Israel Inst. of Technology, Haifa, Israel, 27–28 Feb. 2008.

[29] McLemore, H. C., and Cannon, C. M., "Aerodynamic Investigation of a Four-Blade Propeller Operating Through an Angle-of-Attack Range from 0° to 180°," NACA TN-3228, 1954.

[30] Gur, O., and Rosen, A., "Propeller Performance at Low Advance Ratio," *Journal of Aircraft*, Vol. 42, No. 2, 2004, pp. 435–441.

[31] Rosen, A., "Approximate Actuator Disk Model of a Rotor in Hover or Axial Flow Based on Potential Flow Equations," *Journal of the American Helicopter Society*, Vol. 49, No. 1, 2004, pp. 80–92.

[32] Karamcheti, K., *Principles of Ideal-Fluid Aerodynamics*, 2nd ed., Wiley, New York, 1966.

[33] Gregory, N., and O'Reilly, C. L., "Low Speed Aerodynamic Characteristics of NACA-0012 Aerofoil Section, Including the Effects of Upper-Surface Roughness Simulating Hoar-Frost," Aeronautical Research Council Reports and Memoranda No. 3762, London, Jan. 1970.

[34] McCullough, B. G., and Gault, E. D., "Examples of Three Representative Types of Airfoil Section Stall At Low Speed," NACA TN 2502, Sept. 1951.

[35] Gradshteyn, L. S., and Ryzhik, I. M., *Table of Integrals, Series, and Products*, 2nd ed., Academic Press, New York, 1980.

J. Wei
Associate Editor